chemosensors

MDPI

*Article*

# Pt-Functionalized $SnO_2$ Hollow Nanotubular Structures for $H_2S$ Sensing: Experimental Investigation and DFT Insights

**Hui Li [1,*], Yuhao Qiu [1,2], Xuxu Wang [1], Banglei Liang [1], Zongtao Wang [1], Yingying Dong [1] and Qiao Feng [1,*]**

[1] College of Materials and Chemical Engineering, Henan University of Urban Construction, Pingdingshan 467041, China; 2024521317@link.tyut.edu.cn (Y.Q.); 102423122@huuc.edu.cn (X.W.); 20181028@huuc.edu.cn (B.L.); ztwang@huuc.edu.cn (Z.W.); 20131014@huuc.edu.cn (Y.D.)
[2] College of Textile Engineering, Taiyuan University of Technology, Taiyuan 030024, China
* Correspondence: huuc_lihui@huuc.edu.cn (H.L.); 30100602@huuc.edu.cn (Q.F.)

## Abstract

Pt-functionalized $SnO_2$ hollow nanotubular structures were fabricated by single-nozzle electrospinning followed by calcination and evaluated for $H_2S$ sensing. At an operating temperature of 350 °C, the 2 wt% Pt/$SnO_2$ sensor exhibited a response of 567.1 to 50 ppm $H_2S$, which was 11.9 times higher than that of pristine $SnO_2$. The sensor showed response and recovery times of approximately 1 and 150 s, respectively, an experimental detection limit of 200 ppb, as well as excellent selectivity, repeatability, and long-term stability. Experimental characterizations and DFT calculations indicated that the improved performance arises from the accessible gas-diffusion pathways of the hollow nanotubular structure, together with Pt-enhanced $H_2S$ adsorption and interfacial electronic modulation. In a proof-of-concept shrimp storage test, the sensor response changed consistently with pH, color difference, and sensory scores, with a marked response increase near the observed transition in freshness indicators. These findings demonstrate the potential of Pt/$SnO_2$ HNTSs for $H_2S$ sensing and non-destructive shrimp freshness monitoring.

**Keywords:** Pt-functionalized $SnO_2$; hollow nanotubular structures; $H_2S$ sensing; electrospinning; density functional theory; shrimp freshness monitoring

## 1. Introduction

Hydrogen sulfide ($H_2S$) is a flammable, toxic, and reducing gas generated not only in industrial settings, including petroleum refining, coal gasification, and wastewater treatment, but also as a critical metabolic byproduct of biological decay [1–3]. In aquatic food matrices, particularly fresh shrimp, specific spoilage organisms (e.g., *Shewanella putrefaciens* and *Pseudomonas* spp.) catabolize sulfur-containing amino acids into volatile sulfur compounds during the early stages of storage [4,5]. Among these metabolites, trace $H_2S$ evolves well before overt visual discoloration or olfactory deterioration occurs [6,7]. Conventional freshness assessment of aquatic products still relies predominantly on sensory evaluation and laboratory-based physicochemical or microbiological assays. These include determinations of total volatile basic nitrogen, total viable counts, K-value, pH, and color [8–10], as well as chromatographic platforms and AI-integrated advanced spectroscopic techniques [11,12]. Consequently, rapid and non-destructive gas sensors capable of selectively detecting trace $H_2S$ are of practical significance for food quality surveillance and environmental safety [13].

Check for updates

Received: 13 September 2026
Revised: 1 October 2026
Accepted: 8 October 2026
Published: 10 October 2026

**Copyright:** © 2026 by the authors. Licensee MDPI, Basel, Switzerland. This article is an open access article distributed under the terms and conditions of the Creative Commons Attribution (CC BY) license.

Chemiresistive semiconducting metal oxides (SMOs) sensors have emerged as ideal candidates for non-destructive food quality inspection, largely owing to their compact dimensions, ease of integration, cost-effectiveness, and real-time response capabilities [14–19]. In particular, tin dioxide ($SnO_2$), a classic n-type semiconductor, has been widely used for detecting reducing gases and volatile organic compounds because of its good chemical stability and high electron mobility. Nevertheless, pristine $SnO_2$ generally suffers from insufficient sensitivity, sluggish response kinetics, and inadequate selectivity toward trace target gases [20], which limits its application in complex food headspace. Nanostructure engineering has been extensively explored to address these problems, and electrospun hollow nanotubular structures (HNTSs) are among the most studied morphologies [21–23]. Compared with solid nanofibers or aggregated nanoparticles, HNTSs offer accessible inner and outer surfaces, thin porous walls, and continuous electron-transport pathways, which increase the number of active sites and facilitate gas diffusion, thereby accelerating the response and recovery [24,25]. However, the improvement brought by structural design is largely non-specific, and further enhancement of the response and discrimination toward a target gas generally relies on the catalytic functionalization of the oxide surface.

In this regard, surface functionalization with noble metals represents a particularly effective strategy to tailor the sensing performance of SMOs [26]. Among various catalysts, Pt species are known to activate molecular oxygen into highly reactive chemisorbed oxygen species through catalytic spillover, while significantly lowering the activation energy barrier for $H_2S$ dissociation and surface redox reactions [27,28]. Accordingly, Pt-functionalized $SnO_2$ architectures with diverse geometries have been widely investigated for $H_2S$ detection. For instance, Pt-decorated mesoporous $SnO_2$ nanoflowers delivered a response of 160 to 5 ppm $H_2S$ at 30 °C with a 100 ppb detection limit [29], while Pt nanoparticles supported on $SnO_2$ hierarchical microspheres [30] and nanofibers [31] likewise demonstrated distinctly amplified responses to trace $H_2S$. In these studies, the enhanced performance is commonly discussed in terms of the chemical and electronic sensitization of Pt. However, while these general sensitization pathways explain overall reactivity toward reducing gases, they do not account for the selective recognition of $H_2S$ over other coexisting interferents, which fundamentally hinges on differences in their surface adsorption behavior [32,33]. To bridge this gap, examining the relative adsorption affinities of target and interfering molecules on the modified surface can offer valuable molecular-level clues to help interpret sensor selectivity, particularly for food freshness assessment, where detecting trace $H_2S$ often encounters interference from complex headspace backgrounds.

In this work, Pt-functionalized $SnO_2$ hollow nanotubular structures were prepared by single-nozzle electrospinning followed by calcination. The crystal structure, morphology, elemental composition, and chemical states of the resulting materials were systematically characterized. Their gas-sensing properties were evaluated in terms of operating temperature, response, response–recovery behavior, detection limit, selectivity, repeatability, and long-term stability. The sensing mechanism was further examined through a combination of experimental characterization and density functional theory (DFT) calculations, with particular emphasis on the preferential adsorption of $H_2S$ over common interferents and the interfacial electronic modulation induced by Pt functionalization. Furthermore, as a proof-of-concept demonstration, the sensor was successfully applied to monitor shrimp spoilage, highlighting its practical feasibility for freshness evaluation.

## 2. Experimental

### *2.1. Chemicals and Reagents*

Tin chloride dihydrate ($SnCl_2 \cdot 2H_2O$) and platinum tetrachloride ($PtCl_4$) were purchased from Tianjin Beilian Fine Chemicals Co., Ltd. (Tianjin, China). Polyvinylpyrrolidone

(PVP, (Mw = 1,300,000)) was purchased from Aladdin Reagent Co., Ltd (Shanghai, China). Polyacrylonitrile (PAN, (Mw = 200,000)), N,N-dimethylformamide (DMF) and Ethanol ($C_2H_5OH$) were purchased from Tianjin Fuqi Chemical Co., Ltd. (Tianjin, China). All chemicals were of analytical grade and used as received without further purification. Deionized water was used throughout the experiments.

### *2.2. Fabrication of Pt-Functionalized $SnO_2$ HNTSs*

The synthesis procedure of Pt/$SnO_2$ HNTSs is schematically illustrated in Figure 1. In a typical synthesis, $SnCl_2 \cdot 2H_2O$ (0.2 g) and PAN (0.5 g) were dissolved in 10 mL of DMF under magnetic stirring at room temperature for 1 h. Separately, $PtCl_4$ and 0.5 g of PVP were dissolved in 5 mL of DMF under magnetic stirring at room temperature for 1 h until complete dissolution. The amounts of $PtCl_4$ were set to 1.2 mg, 2.3 mg, 4.6 mg, and 9.2 mg, corresponding to nominal Pt loadings of 0.5 wt%, 1 wt%, 2 wt%, and 4 wt% relative to theoretical $SnO_2$. For comparison, the sample with 0 wt% Pt loading was prepared following the same procedure without adding $PtCl_4$. The two solutions were mixed and further stirred in a water bath at 75 °C for 3 h to obtain a homogeneous spinning precursor. The precursor solution was transferred into a 10 mL plastic syringe fitted with a 21-gauge stainless-steel needle. Electrospinning was conducted at an applied voltage of 13 kV, with a negative bias voltage of −1.5 kV, a needle-to-collector distance of 150 mm, and a solution feed rate of 0.072 mL/min. The ambient temperature and relative humidity were maintained at 25 ± 2 °C and 30 ± 5%, respectively. Finally, the collected precursor nanofibers were placed in a tube furnace and calcined at 700 °C for 1 h at a heating rate of 1 °C $min^{-1}$ to obtain the Pt/$SnO_2$ samples.

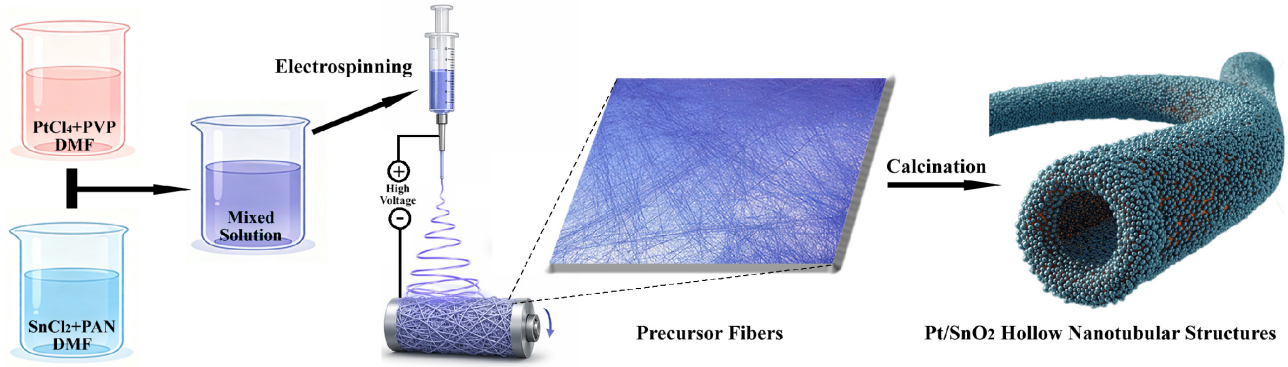



**Figure 1.** Schematic illustration of the procedure for synthesis of Pt/$SnO_2$ HNTSs.

### *2.3. Characterization*

The thermal decomposition behavior and phase evolution of the as-spun precursor nanofibers were investigated by thermogravimetric analysis (TGA). Measurements were performed on a thermal analyzer ( TGA/SDTA 851 MOD, Mettler-Toledo, Greifensee, Switzerland ) in an air atmosphere over a temperature range of 30 to 600 °C with a heating rate of 10 °C/min. After calcination, the crystal structures of the pristine and Pt/$SnO_2$ nanofiber samples were characterized by X-ray diffraction (XRD) on a diffractometer (X'Pert Pro, PANalytical, Almelo, The Netherlands) using Cu Kα radiation (λ = 1.54178 Å). A scan rate of 10°/min was used to record the patterns in the range of 20~80°. The morphologies and microstructures of the samples were examined by scanning electron microscopy (SEM, Hitachi S4800, Hitachi, Tokyo, Japan) and transmission electron microscopy (TEM, JEM-2100, JEOL Ltd., Tokyo, Japan). Energy-dispersive X-ray spectroscopy (EDS) and elemental mapping were employed to analyze the elemental composition and the spatial distribution of Pt, Sn, and O. Selected-area electron diffraction (SAED) patterns were collected during the TEM observations to further confirm the crystallinity and crystalline phase of the

nanofibers. The surface elemental compositions and chemical states were determined by X-ray photoelectron spectroscopy (XPS, Thermo Fisher Scientific, Waltham, MA, USA) using an Al Kα X-ray source (hν = 1486.6 eV).

### *2.4. Gas Sensor Fabrication and Gas Sensing Properties Test*

The fabrication process of the gas sensors was carried out according to the literature [34]. Briefly, the as-prepared sensing material was mildly dispersed in an appropriate amount of anhydrous ethanol to form a homogeneous slurry. The slurry was subsequently brush-coated uniformly onto the outer surface of an alumina ceramic tube (length: 4 mm, outer diameter: 1.2 mm, inner diameter: 0.9 mm). The ceramic tube was pre-equipped with a pair of Au electrodes (electrode gap: ~1.15 mm) and four Pt lead wires. To provide internal heating, a Ni-Cr wire was inserted through the lumen of the ceramic tube to serve as an integrated heater. The coated devices were vacuum-dried at 80 °C for 12 h and then aged at 250 °C for 24 h before testing. The sensor fabrication workflow, device architecture, and test system are schematically shown in Figure S1. Dynamic gas-sensing properties were evaluated using a WS-30A test system (Winsen Electronics, Zhengzhou, China) via a static gas-injection method. After the baseline resistance stabilized in the sealed chamber, a defined volume of target gas was injected via a microsyringe with rapid fan-assisted mixing. Sensor resistance was continuously recorded in real time until reaching steady state, after which the chamber was opened to ambient air to record the recovery transient. The operating temperature of the sensors was investigated in the range of 250–390 °C, which was regulated by adjusting the heating voltage applied across the built-in Ni-Cr heating wire. The relative humidity inside the test chamber was adjusted between 30% and 80% RH by injecting calculated amounts of deionized water into the evaporator, and the actual RH values were recorded in real time using the built-in humidity sensor, similar to previous reports [35]. During dynamic sensing measurements, once the baseline resistance stabilized in air, a defined volume of target gas was injected into the sealed chamber using a microsyringe. After the sensor resistance reached a steady state, the chamber was opened to ambient air to allow the sensor to recover. For reducing gases, which reduce the resistance of the sensors, the Response (S) is calculated using S = Ra/Rg, where Ra is the sensor resistance in air and Rg is the sensor resistance in the test gas. The response and recovery times of the sensor are defined as the time intervals required to achieve 90% of the total resistance variation upon exposure to the target gas and upon subsequent recovery in air, respectively.

### *2.5. Density Functional Theory Calculation*

Using first-principles DFT computations, the adsorption behavior of $H_2S$ on pristine and Pt-functionalized $SnO_2$(110) surfaces was systematically investigated. The $SnO_2$(110) surface was modeled using a 2 × 2 supercell with dimensions of a = 6.45 Å, b = 13.59 Å and c = 24.43 Å, constructed from the optimized bulk rutile lattice (a = 4.805 Å, c = 3.225 Å). For the decorated surface, a single Pt atom was substituted into a surface five-fold coordinated Sn (Sn5c) site [36]. All simulations were performed using the CASTEP module implemented in Materials Studio (version 2024). The exchange-correlation functional was described by the generalized gradient approximation with the Perdew-Burke-Ernzerhof parameterization. A plane-wave cutoff energy of 500 eV and a 4 × 2 × 1 Monkhorst-Pack k-point grid were selected for Brillouin zone integration, while a 15 Å vacuum layer was introduced along the z-axis to avoid interactions between periodic slabs [37,38]. The 4 × 2 in-plane sampling provides comparable k-point densities along the a and b directions, given that b is approximately twice the length of a. The convergence of the k-point grid was verified with respect to the total energy, which changed by only 1.53 meV/atom when

the grid was increased to 6 × 3 × 1. To elucidate the Pt-promoted gas-sensing mechanism, the adsorption energy ($E_{ads}$), density of states (DOS), partial density of states (PDOS), and electron density difference were thoroughly analyzed.

### *2.6. Practical Freshness Evaluation of Shrimp*

To assess the practical capability of the Pt/$SnO_2$ HNTSs sensor, fresh shrimp samples were sealed in a container maintained at 30 °C for a 24 h spoilage study. At designated intervals (0, 2, 4, 6, 8, 12, and 24 h), the accumulated headspace gas was sampled with an airtight syringe and injected into the gas-sensing system to record dynamic sensor responses. Simultaneously, shrimp surface exudate pH was directly monitored using precision pH test strips. Colorimetric changes in calibrated sample photographs were quantified via ImageJ (version 1.54t) to extract $L^*$, $a^*$, and $b^*$ coordinates, yielding the total color difference ($\Delta E$) relative to the initial state according to the following Equation (1), where $L^*$ is the lightness component, $a^*$ is the red–green component, and $b^*$ is the yellow–blue component [39].

$$\Delta E = \sqrt{(L^* - L_0^*)^2 + (a^* - a_0^*)^2 + (b^* - b_0^*)^2} \quad (1)$$

Sensory quality was evaluated using a 10-point descriptive scale covering tissue elasticity, odor, and shell discoloration, with scores below 6 indicating initial spoilage [40].

## 3. Results and Discussion

### *3.1. Morphological and Microstructural Evolution*

The morphological evolution from electrospun precursor fibers to the final heterostructured product was systematically investigated by SEM and TEM (Figure 2). As shown in Figure 2a, the as-spun precursor consists of continuous fibers with smooth surfaces and a uniform diameter distribution. The enlarged SEM image (inset of Figure 2a) further confirms the absence of discernible particles or structural defects, suggesting the homogeneous dispersion of the PVP and PAN matrix and tin oxide precursors in the electrospun fibers. After calcination, the smooth precursor fibers are converted into rough and porous hollow nanofibers assembled from interconnected nanoparticles (Figure 2b). The formation of the hollow architecture is associated with the thermal decomposition of the PVP/PAN matrix and the release of gaseous products during calcination. As supported by the thermal analysis (Figure S2), substantial polymer decomposition occurs at approximately 240–300 °C and proceeds with increasing temperature. Meanwhile, the conversion, migration, and reorganization of Sn-containing species during polymer removal promote the formation of an inorganic shell and the development of an internal void. Upon complete elimination of the polymer scaffold at elevated temperatures, the remaining $SnO_2$ and Pt-containing nanoparticles interconnect to form a porous Pt/$SnO_2$ hollow nanotubular structure framework. This thermally induced decomposition–mass transport process has been widely recognized as an effective route for constructing hollow nanotubular structures from single-nozzle electrospun precursor fibers [41,42]. The inset of Figure 2b clearly reveals the ruptured end of a single hollow tubular structure, highlighting a well-defined tubular structure with a porous shell composed of aggregated primary nanoparticles. The outer diameter shrinks to 150–200 nm with a shell thickness of 30–50 nm. Such a thin and porous shell allows gas molecules to access both the inner and outer surfaces of the tubes.

SEM-EDS elemental mapping was performed to examine the spatial distribution of the constituent elements in the 2 wt% Pt/$SnO_2$ HNTSs (Figure 2c). Sn, O, and Pt signals are detected throughout the fibrous region, indicating the successful incorporation of Pt into the $SnO_2$ hollow nanotubular framework. No pronounced microscale Pt-rich domains are observed, suggesting the uniform functionalization of Pt on the $SnO_2$ host.

The corresponding SEM-EDS spectrum (Figure S3) further confirms the presence of Sn, O, and Pt in Pt/$SnO_2$.

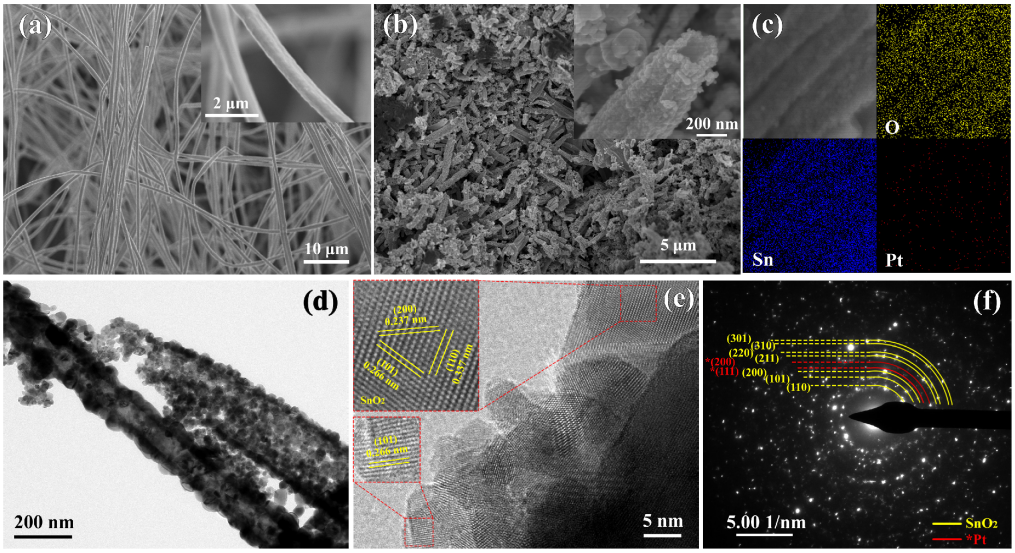



**Figure 2.** Morphological and structural characterization of the electrospun precursor and 2 wt% Pt/$SnO_2$ HNTSs: (**a**) SEM image of the as-spun precursor fibers, with a magnified view in the inset; (**b**) SEM image of the 2 wt% Pt/$SnO_2$ HNTSs after calcination, with a magnified image of a ruptured fiber end in the inset; (**c**) SEM-EDS elemental mapping of Sn, O, and Pt; (**d**) TEM image showing the continuous hollow tubular structure; (**e**) HRTEM image with lattice spacings characteristic of rutile $SnO_2$; and (**f**) SAED pattern, with yellow and red rings indexed to $SnO_2$ and metallic Pt, respectively.

Further 2 wt% Pt/$SnO_2$ HNTSs structural details were studied via TEM characterizations. The TEM image (Figure 2d) confirms the continuous 1D hollow morphology. The strong mass-thickness contrast between the bright inner channel and the dark shell edge offers unambiguous evidence of the hollow tubular interior. It is found that the shell wall is not a dense single crystal, but is constructed by the self-assembly and tight intergrowth of polycrystalline nanoparticles, creating abundant permeable grain boundaries and porosity. In the high-resolution TEM image (Figure 2e), well-defined lattice fringes demonstrate high crystallinity. The d-spacings of 0.337 nm, 0.266 nm, and 0.237 nm in the major matrix correspond to the (110), (101), and (200) crystallographic planes of tetragonal rutile $SnO_2$, respectively. Notably, no distinct lattice fringes that can be unambiguously assigned to Pt are resolved in the selected high-resolution TEM region, suggesting that the Pt-containing species are not readily distinguishable at the present imaging condition. The selected area electron diffraction (SAED) pattern (Figure 2f) displays a series of bright, concentric diffraction rings, confirming the polycrystalline nature of the Pt/$SnO_2$ HNTSs. The yellow rings are indexed to the (110), (101), (200), (211), (220), (310), and (301) planes of $SnO_2$, while the distinct red rings correspond to the (111) and (200) planes of face-centered cubic metallic Pt. The chemical state and structural nature of Pt species are further clarified by the subsequent diffraction and spectroscopic analyses.

### *3.2. Structural and Chemical Characterization*

The crystallographic structure and phase evolution of the as-prepared precursor fibers, pure $SnO_2$, and 2 wt% Pt/$SnO_2$ HNTSs were investigated by XRD, as depicted in Figure 3a. The XRD pattern of the as-spun precursor fibers exhibits a broad diffuse feature rather than well-resolved Bragg reflections. This diffraction behavior is characteristic of the predominantly amorphous or poorly ordered PVP/PAN polymer matrix, which constitutes the major fraction of the precursor fibers. No distinct reflections associated with

crystalline $SnO_2$, metallic Pt, or other inorganic phases are observed, indicating that the Sn and Pt precursors are molecularly dispersed or present as poorly crystallized species within the polymeric matrix prior to calcination. Upon thermal treatment, both $SnO_2$ HNTSs and 2 wt% Pt/$SnO_2$ HNTSs display sharp and well-defined diffraction peaks at 2θ = 26.6°, 33.8°, 37.9°, 51.8°, 54.8°, 57.8°, 61.9°, 64.7° and 65.9°, corresponding to the (110), (101), (200), (211), (220), (002), (310), (112), and (301) planes of tetragonal cassiterite $SnO_2$ (JCPDS No. 41-1445), respectively. For the 2 wt% Pt/$SnO_2$ HNTSs, additional subtle yet distinct reflections emerge at 2θ = 39.8°, 46.2°, and 67.5°, which are unambiguously indexed to the (111), (200), and (220) crystal planes of metallic Pt (JCPDS No. 04-0802). No diffraction peaks of crystalline platinum oxides or Sn–Pt intermetallic compounds are detected, indicating that the crystalline Pt phase is metallic $Pt^0$. Oxidized Pt species present as a thin surface layer or in an amorphous state are below the detection limit of XRD and are further examined by XPS below. Furthermore, the peak positions of the $SnO_2$ host remain virtually unchanged after Pt introduction, suggesting that Pt is loaded on the $SnO_2$ surface rather than incorporated into its crystal lattice. These results indicate that Pt loading leaves the $SnO_2$ host structure intact. Any change in sensing performance (Section 3.3) is therefore expected to stem from the surface Pt species and the Pt/$SnO_2$ interfaces rather than from modification of the $SnO_2$ lattice.

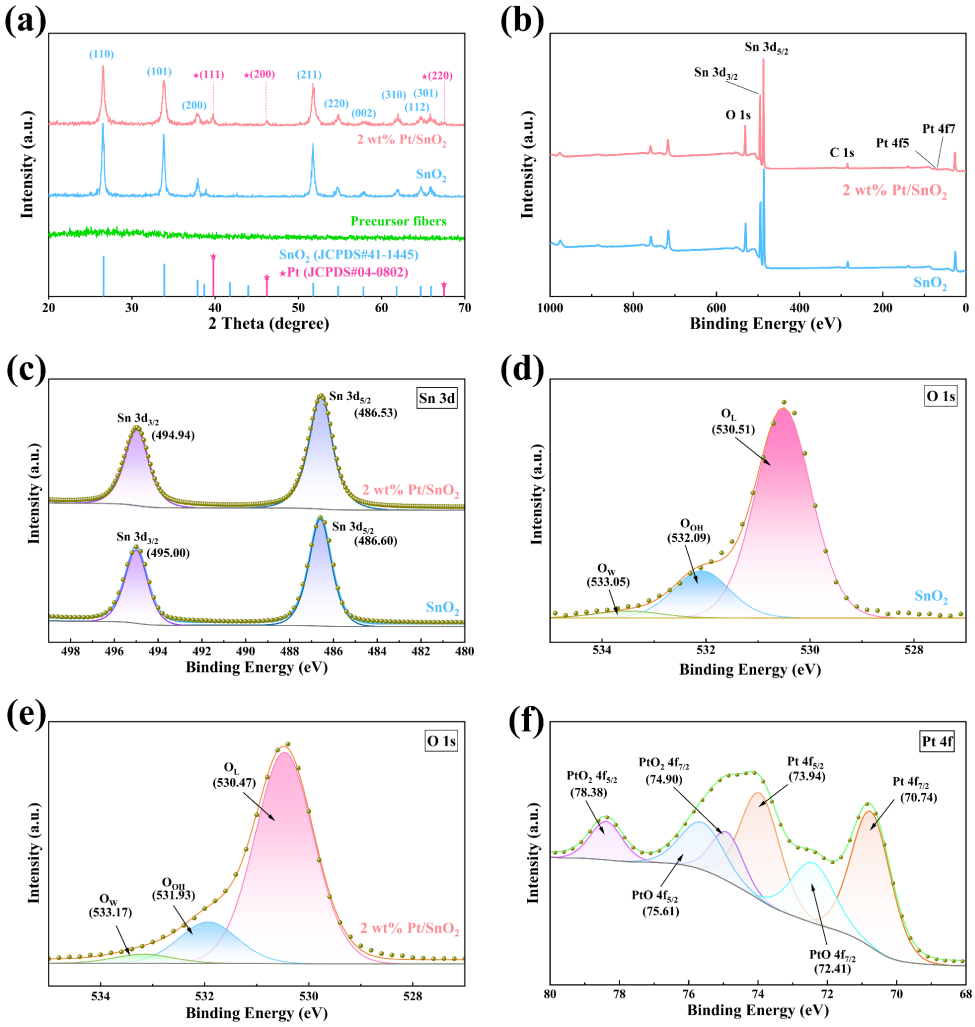



**Figure 3.** Structural and surface chemical characterization of $SnO_2$ and 2 wt% Pt/$SnO_2$: (**a**) XRD patterns of the precursor fibers, $SnO_2$, and 2 wt% Pt/$SnO_2$ HNTSs; (**b**) XPS survey spectra; (**c**) high-resolution Sn 3d spectra; (**d**,**e**) high-resolution O 1s spectra of $SnO_2$ and 2 wt% Pt/$SnO_2$ HNTSs, respectively; and (**f**) high-resolution Pt 4f spectrum of 2 wt% Pt/$SnO_2$ HNTSs.

XPS survey and high-resolution spectra were collected to investigate surface chemical states. The survey spectrum (Figure 3b) verifies the coexistence of Sn, O, C, and Pt elements in the Pt/$SnO_2$ composite, consistent with the EDS results. The surface atomic ratios of Sn, O and Pt obtained from the survey spectra, as well as the relative contents of the O and Pt species derived from the deconvoluted high-resolution spectra, are summarized in Table S1. The survey spectrum confirms the presence of Sn, O, and Pt without other impurity elements, so the sensing properties discussed below are not affected by foreign contaminants. The high-resolution Sn 3d spectra (Figure 3c) display two symmetric peaks corresponding to Sn $3d_{5/2}$ and Sn $3d_{3/2}$. For pure $SnO_2$ HNTSs, these peaks appear at 486.60 eV and 495.00 eV, characteristic of the $Sn^{4+}$ state in rutile $SnO_2$. The Sn $3d_{5/2}$ and Sn $3d_{3/2}$ peaks at 486.53 and 494.94 eV are characteristic of $Sn^{4+}$, and no obvious shift is observed after Pt loading. The unchanged $Sn^{4+}$ signals indicate that the chemical state of the $SnO_2$ host is preserved. Consequently, any electronic influence of Pt on $SnO_2$ should be confined to the Pt/$SnO_2$ interface rather than arise from lattice doping. The O 1s spectra of $SnO_2$ and 2wt% Pt/$SnO_2$ (Figure 3d,e) were deconvoluted into three components. The peak at 530.51 eV is assigned to lattice oxygen ($O_L$) in $SnO_2$, and the peaks at 532.09 and 533.05 eV are attributed to surface hydroxyl groups ($O_{OH}$) and adsorbed molecular water ($O_W$), respectively [43–45]. The comparable fractions of the oxygen species in the two samples (Table S1) suggest that Pt loading does not noticeably increase the oxygen vacancies or chemisorbed oxygen at room temperature. The effect of Pt on oxygen adsorption is thus more likely to manifest at elevated temperatures, where Pt can dissociate $O_2$ and spill the activated oxygen over onto the $SnO_2$ surface.

The high-resolution Pt 4f spectrum (Figure 3f) was deconvoluted to determine the surface chemical states of Pt. The spectrum can be fitted with three Pt 4f spin–orbit doublets, corresponding to $Pt^0$, $Pt^{2+}$, and $Pt^{4+}$ species. The doublet located at approximately 70.74 eV (Pt $4f_{7/2}$) and 73.94 eV (Pt $4f_{5/2}$) is assigned to metallic $Pt^0$. The components centered at approximately 72.41 and 75.61 eV are attributed to $Pt^{2+}$ species, which can be associated with PtO-related surface species. The higher-binding-energy doublet located at approximately 74.90 and 78.38 eV is assigned to $Pt^{4+}$ species, indicating the presence of more highly oxidized $PtO_2$ species. The relative proportions of $Pt^0$, $Pt^{2+}$, and $Pt^{4+}$ were estimated to be 56.37%, 27.19%, and 16.44%, respectively.

These results confirm that Pt is present on the $SnO_2$ HNTSs as mixed metallic $Pt^0$ and oxidized $PtO_x$ surface species, rather than as a purely metallic phase. The oxidized Pt species may originate from partial oxidation during thermal treatment and subsequent exposure to air, while their stabilization may also be related to the interfacial interaction between Pt-containing species and the $SnO_2$ support. Although Pt-related lattice fringes were not directly observed in the selected high-resolution TEM image, the successful incorporation of Pt is consistently supported by EDS spectrum and elemental mapping, XRD, SAED and XPS. Such Pt-containing species and their interface with $SnO_2$ are expected to facilitate gas adsorption, surface oxygen activation, and interfacial charge transfer, which provides the basis for interpreting the sensing behavior below.

### *3.3. Gas-Sensing Performance*

The operating temperature is one of the most critical parameters governing the performance of metal-oxide-based chemiresistive sensors, as it directly influences the surface reaction kinetics, oxygen adsorption behavior, and carrier transport. The responses of the $SnO_2$ and Pt/$SnO_2$ HNTSs with different Pt contents toward 50 ppm $H_2S$ were therefore evaluated over the temperature range of 250–390 °C (Figure 4a). For all samples, the response first increases and then decreases with increasing temperature, exhibiting a typical volcano-shaped dependence. This behavior can be attributed to the competition between

the enhanced surface reaction kinetics and the reduced gas adsorption capacity at elevated temperatures. All Pt/$SnO_2$ HNTSs samples reach their maximum response at 350 °C, which is thus selected as the optimal operating temperature for subsequent measurements.

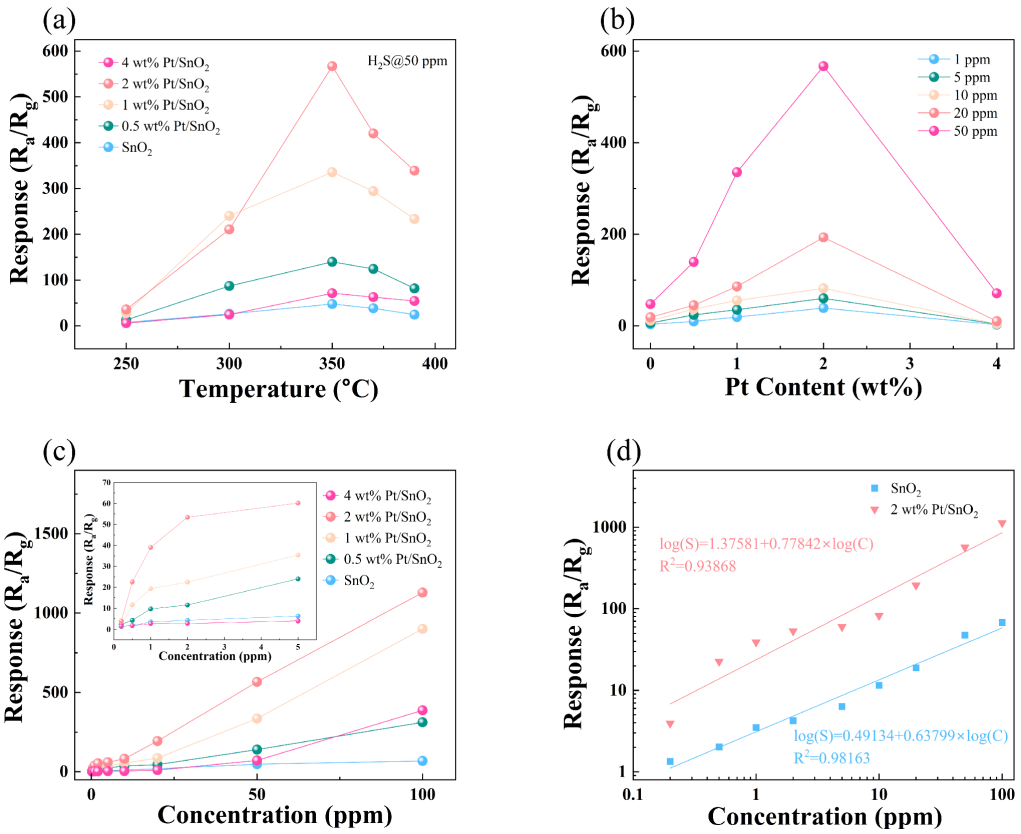



**Figure 4.** Gas-sensing performance of $SnO_2$ and Pt/$SnO_2$ HNTSs toward $H_2S$. (**a**) Responses of $SnO_2$ and Pt/$SnO_2$ HNTSs with different Pt loadings toward 50 ppm $H_2S$ at different operating temperatures. (**b**) Responses of the samples with different Pt contents to various $H_2S$ concentrations at 350 °C. (**c**) Responses of all samples as a function of $H_2S$ concentration at 350 °C (inset: low-concentration region). (**d**) Double-logarithmic fitting plots of response versus $H_2S$ concentration for $SnO_2$ and 2 wt% Pt/$SnO_2$ HNTSs.

The effect of Pt loading was further examined at 350 °C under different $H_2S$ concentrations (Figure 4b). The response increases as the Pt content increases from 0 to 2 wt%, but decreases markedly when the Pt content is further raised to 4 wt%. The 2 wt% Pt/$SnO_2$ HNTSs exhibit the highest response across all concentrations, indicating an optimal Pt loading. At this load, Pt is uniformly distributed over the hollow nanotubular structures without microscale Pt-rich domains (Figure 2c), thus providing abundant Pt/$SnO_2$ interfaces as active sites. In contrast, excessive Pt may cover the active $SnO_2$ surface or aggregate into larger particles [46,47], reducing the effective interfaces.

Figure 4c illustrates the response of $SnO_2$ and Pt/$SnO_2$ sensors as a function of $H_2S$ concentration ranging from 0.2 to 100 ppm at 350 °C. The response of all samples increases monotonically with increasing gas concentration. In particular, the 2 wt% Pt/$SnO_2$ HNTSs show a markedly enhanced response throughout the investigated concentration range, achieving response values of approximately 567.1 toward 50 ppm $H_2S$, which is 11.9 times higher than that of pristine $SnO_2$. The inset of Figure 4c highlights the excellent sensing capability at low gas concentrations (0.2–5 ppm), where the 2 wt% Pt/$SnO_2$ HNTSs sensor still exhibits a response of 3.93 to 200 ppb $H_2S$. To further clarify the power-law relationship characteristic of SMOs gas sensors, the double-logarithmic curves of response versus concentration are plotted in Figure 4d. In the concentration range of 0.2–100 ppm,

both 2 wt% Pt/$SnO_2$ and pristine $SnO_2$ sensors exhibit good linear behavior in log–log coordinates. The fitted linear equations are determined to be:

$$\log(S) = 1.37581 + 0.77842 \times \log(C) \quad (R^2 = 0.93868) \tag{2}$$

for 2 wt% Pt/$SnO_2$ HNTSs Equation (2), and

$$\log(S) = 0.49134 + 0.63799 \times \log(C) \quad (R^2 = 0.98163) \tag{3}$$

for pristine $SnO_2$ HNTSs Equation (3), where S and C denote the sensor response and gas concentration, respectively. The higher slope and intercept of the 2 wt% Pt/$SnO_2$ HNTSs indicate a higher sensitivity and stronger response dependence on $H_2S$ concentration compared with the pristine $SnO_2$. The good linearity over a wide concentration range suggests that the 2 wt% Pt/$SnO_2$ HNTSs are promising for quantitative $H_2S$ detection.

The dynamic response-recovery curves of all samples toward $H_2S$ at concentrations ranging from 1 to 50 ppm at 350 °C are shown in Figure 5a. Each sample exhibits stepwise and reversible response signals upon successive exposure to increasing $H_2S$ concentrations, and the response amplitude increases accordingly. Among all samples, the 2 wt% Pt/$SnO_2$ HNTSs display the largest response at each concentration, consistent with the results in Figure 4b, confirming the superior sensing performance enabled by the optimal Pt loading.

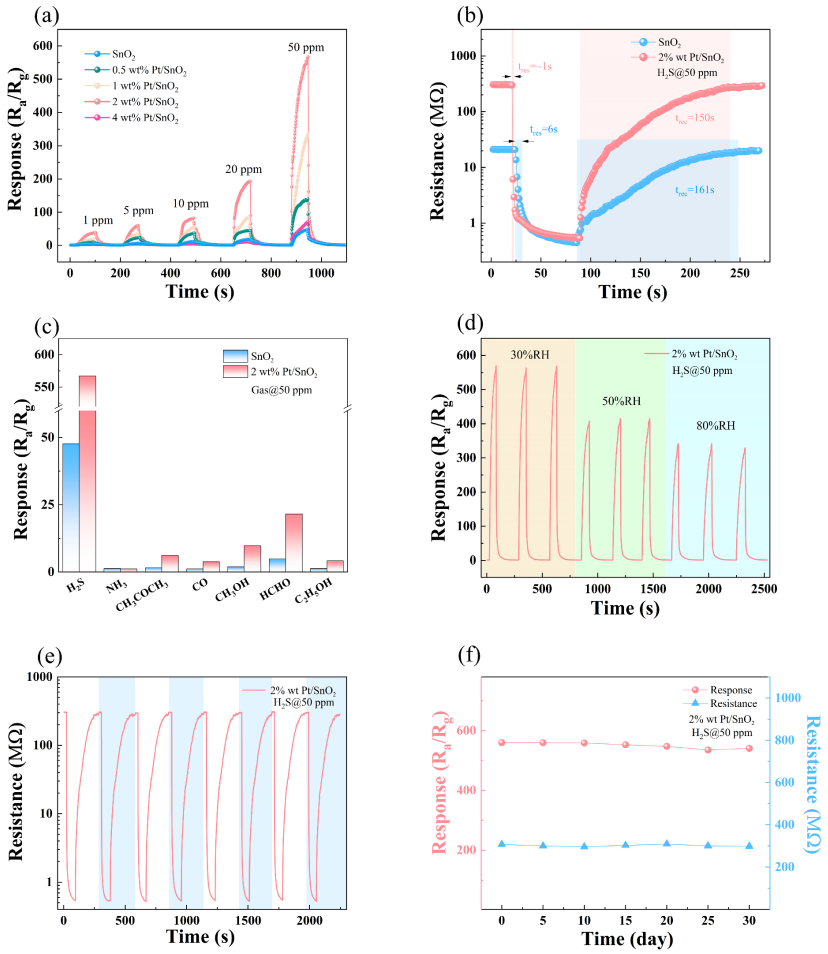



**Figure 5.** Gas sensing performance of the sensors at 350 °C. (**a**) Dynamic response–recovery curves of all samples to various $H_2S$ concentrations. (**b**) Dynamic resistance curves and response/recovery times of pristine and 2 wt% Pt/$SnO_2$ HNTSs to 50 ppm $H_2S$. (**c**) Selectivity of pristine and 2 wt% Pt/$SnO_2$ HNTSs to 50 ppm interfering gases. (**d**) Humidity-dependent response, (**e**) reproducibility, and (**f**) long-term stability of the 2 wt% Pt/$SnO_2$ HNTSs sensor to 50 ppm $H_2S$.

The dynamic resistance response curve toward 50 ppm $H_2S$ was analyzed to extract the response and recovery times (Figure 5b). The 2 wt% Pt/$SnO_2$ show an ultrafast response time of approximately 1 s, which is significantly faster than that of pristine $SnO_2$ (6 s). The remarkably shortened response time confirms the strong catalytic sensitization of Pt nanoparticles in promoting target gas adsorption and surface redox reaction kinetics. Although the 2 wt% Pt/$SnO_2$ HNTSs exhibit a relatively longer recovery time of approximately 150 s than pristine $SnO_2$ (~161 s), their recovery behavior remains acceptable considering the much larger response magnitude toward $H_2S$.

To evaluate the trace-level detection potential, the resistance transient toward sub-ppm $H_2S$ was measured (Figure S4). For 200 ppb $H_2S$, the 2 wt% Pt/$SnO_2$ sensor displays a clear response-recovery signal with an extended response time ($t_{res}$ = 42 s) and a substantially reduced recovery time ($t_{rec}$ = 35 s). The longer response time at ppb levels is ascribed to the sluggish diffusion and low collision frequency of target gas molecules at ultra-low concentrations, whereas the shortened recovery time stems from the rapid desorption of sparse surface-bound species upon gas evacuation.

Good selectivity is one of the basic requirements for a gas sensor to avoid the interference of other gases during the sensing process. To investigate their selectivity, the responses of pristine $SnO_2$ and 2 wt% Pt/$SnO_2$-based sensors to $H_2S$ and other interfering gases, involving $NH_3$, $CH_3COCH_3$, CO, $CH_3OH$, HCHO, and $C_2H_5OH$, were recorded, as shown in Figure 5c. The 2 wt% Pt/$SnO_2$ sensor displays overwhelming selectivity toward $H_2S$, whereas its responses to all other interfering gases remain below 22. This performance yields an exceptionally high selectivity coefficient ranging from 26 to 490 relative to interfering gases, demonstrating that the catalytic modification with Pt selectively accelerates the reaction kinetics of $H_2S$. This pronounced selectivity suggests a preferential interaction between the Pt sites and $H_2S$, which is further examined by DFT calculations in Section 3.4.

The effect of relative humidity on the sensing performance of the 2 wt% Pt/$SnO_2$ HNTSs sensor was further investigated, as shown in Figure 5d. With the relative humidity increasing from 30% to 50% and 80% RH, the response gradually decreases from approximately 567 to 400 and 330, respectively. This reduction is likely associated with the competitive adsorption of water molecules on the sensing surface, which partially suppresses the adsorption and reaction of $H_2S$. Nevertheless, distinct and repeatable response–recovery cycles are retained even at 80% RH, indicating the good humidity tolerance of the sensor.

As presented in Figure 5e, the repeatability of the 2 wt% Pt/$SnO_2$ HNTSs was evaluated by continuously switching between $H_2S$ and air over multiple cycles. The resistance transients remain nearly identical across successive cycles, with a stable baseline and reproducible response amplitude, which highlights the good repeatability and reversibility of the sensor. Finally, as illustrated in Figure 5f, the long-term stability of the 2 wt% Pt/$SnO_2$ HNTSs was investigated over a period of 30 days. Both the gas response and baseline resistance remain essentially unchanged throughout the testing period, exhibiting negligible performance degradation. This outstanding long-term stability further confirms the robustness and practical reliability of the 2 wt% Pt/$SnO_2$ HNTSs for $H_2S$ sensing applications.

Additionally, Table 1 presents a comprehensive comparison of the $H_2S$ sensing performance between the 2 wt% Pt/$SnO_2$ HNTSs sensor in this study and other reported SMOs-based $H_2S$ gas sensors. From this comparison, the 2 wt% Pt/$SnO_2$ HNTSs sensor exhibits highly competitive performance, demonstrating a well-balanced combination of high response, rapid response speed, and a low detection limit down to 200 ppb alongside other well-performing materials. Overall, Pt functionalization markedly enhances the response, accelerates the response kinetics, and endows the sensor with high selectivity toward $H_2S$. The origins of these improvements are discussed in the following section.

**Table 1.** Comparison of $H_2S$ sensing performances of the Pt/$SnO_2$ HNTSs with representative SMOs-based resistive gas sensors.

| Sensing Material | Operating Temp. (°C) | Conc. (ppm) | Response (Ra/Rg) | Response/Recovery Time (s) | Detection Limit (ppb) | Ref. |
|---|---|---|---|---|---|---|
| $SnO_2$ nanofibers | 350 | 1 | 15.2 | 15/230 | 1.6 | [48] |
| ZnO nanorods | 300 | 10 | 116 | 200/600 | 25 | [49] |
| $Ag_2O/SnO_2$ mesoporous | 100 | 1 | 57 | 390/1600 | 50 | [50] |
| Pt/$SnO_2$ hollow spheres | 250 | 1 | 10.8 | 192/77 | 100 | [30] |
| Pd/$SnO_2$ nanostructures | 290 | 50 | 19.87 | 7/10 | 5000 | [51] |
| Au/$SnO_2$ nanospheres | 200 | 10 | 46.81 | 455/315 | 2 | [52] |
| ZnO/$SnO_2$ heterostructure | 450 | 5 | 172 | 37/57 | 300 | [53] |
| $\alpha$-$Fe_2O_3$/ZnO core–shell nanowires | 250 | 5 | 5.98 | 81/43 | 1000 | [54] |
| CuO/$WO_3$ nanowires | 300 | 100 | 79.8 | ~30/200 | 1000 | [55] |
| Cu/$In_2O_3$ HNFs | 250 | 50 | 350.7 | 24/300 | 1000 | [56] |
| Pt/$SnO_2$ HNTSs | 350 | 50 | 567.1 * | ~1/150 | 200 | This work |

* Sensor responses are 3.93 (0.2 ppm), 39.0 (1 ppm), 60.2 (5 ppm), 82.0 (10 ppm), 567.1 (50 ppm), and 1128.7 (100 ppm).

### *3.4. Gas Sensing Mechanism and DFT Calculations*

To explain the enhanced response, faster response, and high $H_2S$ selectivity observed above, the sensing mechanism of the Pt/$SnO_2$ HNTSs is discussed on the basis of the characterization results and DFT calculations. The sensing behavior is governed by surface oxygen adsorption–desorption and the modulation of the space-charge region (Figure 6). When the sensor is exposed to ambient air at an operating temperature of 350 °C, atmospheric oxygen molecules adsorb onto the surface of the tubular $SnO_2$ shell. At this elevated temperature (>300 °C), the adsorbed oxygen captures conduction-band electrons from the $SnO_2$ matrix and sequentially undergoes multi-electron transfer steps ($O_2 \rightarrow O_2^- \rightarrow O^- \rightarrow O^{2-}$), ultimately yielding stable $O^{2-}$ species as described in Equations (4)–(7) [57]:

$$O_2\ (gas) \rightarrow O_2\ (ads) \quad (4)$$

$$O_2\ (ads) + e^- \rightarrow O_2^-\ (ads) \qquad (T \leq 100\ ^\circ C) \quad (5)$$

$$O_2^-\ (ads) + e^- \rightarrow 2O^-(ads) \qquad (100\ ^\circ C < T \leq 300\ ^\circ C) \quad (6)$$

$$O^-\ (ads) + e^- \rightarrow O^{2-}\ (ads) \qquad (T > 300\ ^\circ C) \quad (7)$$

The trapping of free electrons by surface oxygen ions forms a thick Electron Depletion Layer beneath the $SnO_2$ surface [58]. This electron depletion elevates the surface energy band bending, leading to a high potential barrier and causing a substantial increase in the baseline resistance ($R_a$) in air (Figure 6a,c). As shown in Figure 6b, upon exposure to the target reducing gas $H_2S$, the gas molecules interact vigorously with the surface-bound $O^{2-}$ species at 350 °C to generate $SO_2$ and $H_2O$, releasing six trapped electrons back into the conduction band of $SnO_2$ Equation (8):

$$H_2S\ (gas) + 3O^{2-}\ (ads) \rightarrow SO_2\ (gas) + H_2O\ (gas) + 6e^- \quad (8)$$

The massive injection of liberated electrons thins the depletion layer and flattens the energy band bending, markedly diminishing the Schottky-like interfacial potential barrier (Figure 6d). As a result, the sensor resistance drops drastically from $R_a$ to $R_g$, delivering a highly sensitive response to $H_2S$.

The remarkable response enhancement observed in the Pt/$SnO_2$ heterostructure arises from the synergistic coupling of chemical sensitization, electronic sensitization, and structural advantages. From a chemical perspective, the Pt nanoparticles, which exist mainly as metallic $Pt^0$ (Figures 2f and 3a,f), act as effective catalytic centers for oxygen dissociation. Oxygen molecules preferentially adsorb on the Pt surface and break down

into atomic oxygen, which then spills over onto the adjacent $SnO_2$ surface to form abundant ionized oxygen species [59]. This catalytic spillover effect significantly accelerates oxygen dissociation kinetics and boosts surface reactivity toward $H_2S$ oxidation [47]. Although the room-temperature O 1s spectra show little change after Pt loading (Figure 3d,e), this spillover process proceeds at the operating temperature and is consistent with the markedly shortened response time (Figure 5b). From an electronic perspective, because the work function of metallic Pt ($\Phi_{Pt} \approx 5.65$ eV) exceeds that of n-type $SnO_2$ ($\Phi_{SnO2} \approx 4.90$ eV), electrons spontaneously flow from $SnO_2$ to Pt nanoparticles until Fermi level equilibrium is reached. This directional charge transfer establishes localized Schottky barriers at the metal-semiconductor interface, further deepening the baseline depletion layer within the $SnO_2$ matrix. In addition, the oxidized Pt species at the Pt/$SnO_2$ interface (Figure 3f) can also extract electrons from $SnO_2$ [60], further widening the depletion layer. During gas interaction, even minor variations in charge carrier density trigger exponential shifts in Schottky barrier height, effectively boosting resistance modulation [60,61].

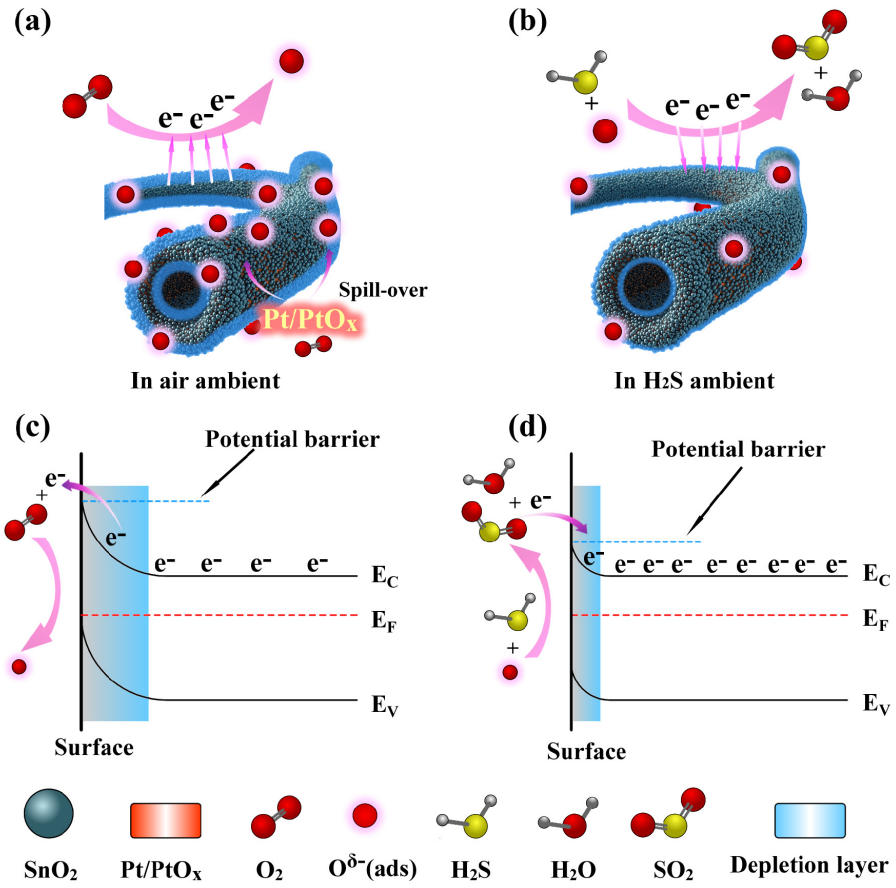



**Figure 6.** Schematic illustration of the $H_2S$-sensing mechanism of Pt/$SnO_2$ HNTSs. (**a**) oxygen adsorption and spill-over effect in air; (**b**) surface reaction with $H_2S$; (**c**) band diagram and depletion layer in air; (**d**) potential barrier reduction in $H_2S$.

The hollow architecture (Figure 2b,d) also plays an important structural role. The open channel exposes both the inner and outer walls to the gas, facilitating rapid gas diffusion [62]. Moreover, the shell consists of interconnected nanoparticles with abundant grain boundaries (Figure 2d). When the grain size is comparable to twice the Debye length of $SnO_2$ the grains can be almost fully depleted, and the grain-boundary barriers are strongly modulated upon gas exposure [22]. This structural feature, shared by both sensors, accounts for the considerable response of pristine $SnO_2$ HNTSs, whereas the further 11.9-fold enhancement arises from Pt functionalization.

To further elucidate the role of Pt modification in regulating $H_2S$ adsorption and interfacial charge transfer, DFT calculations were performed for pristine $SnO_2$(110) and Pt-substituted $SnO_2$(110) surfaces. The Pt/$SnO_2$(110) model was constructed by replacing a five-coordinated surface Sn atom (Sn5c) with a Pt atom (Figure S5). Based on previous reports [36,63], the most stable dissociative adsorption configurations were adopted, in which $H_2S$ is adsorbed at the Sn5c site on pristine $SnO_2$(110) and at the $Pt_{Sn5c}$ site on the Pt-substituted surface. In the optimized structures, one H atom is transferred from $H_2S$ to a neighboring bridging oxygen atom, leading to S–H bond dissociation and the formation of an O–H bond [64].

Figure 7 shows the optimized adsorption configurations of $H_2S$ on pristine $SnO_2$(110) (Figure 7a) and $Pt_{Sn5c}/SnO_2$(110) (Figure 7b). The S atom interacts directly with the surface adsorption center, and the Pt–S distance is 2.333 Å, which is shorter than the corresponding S–Sn5c distance of 2.517 Å on pristine $SnO_2$(110), indicating a stronger local interaction at the Pt site. For the dissociative adsorption configuration, the transferred H atom forms an O–H bond with a bond length of 1.006 Å, whereas the remaining S–H bond is 1.354 Å. Importantly, the distance between the S atom and the dissociated H atom reaches 2.278 Å, substantially larger than the original S–H bond length in molecular $H_2S$ (1.328 Å), confirming the cleavage of one S–H bond during adsorption.

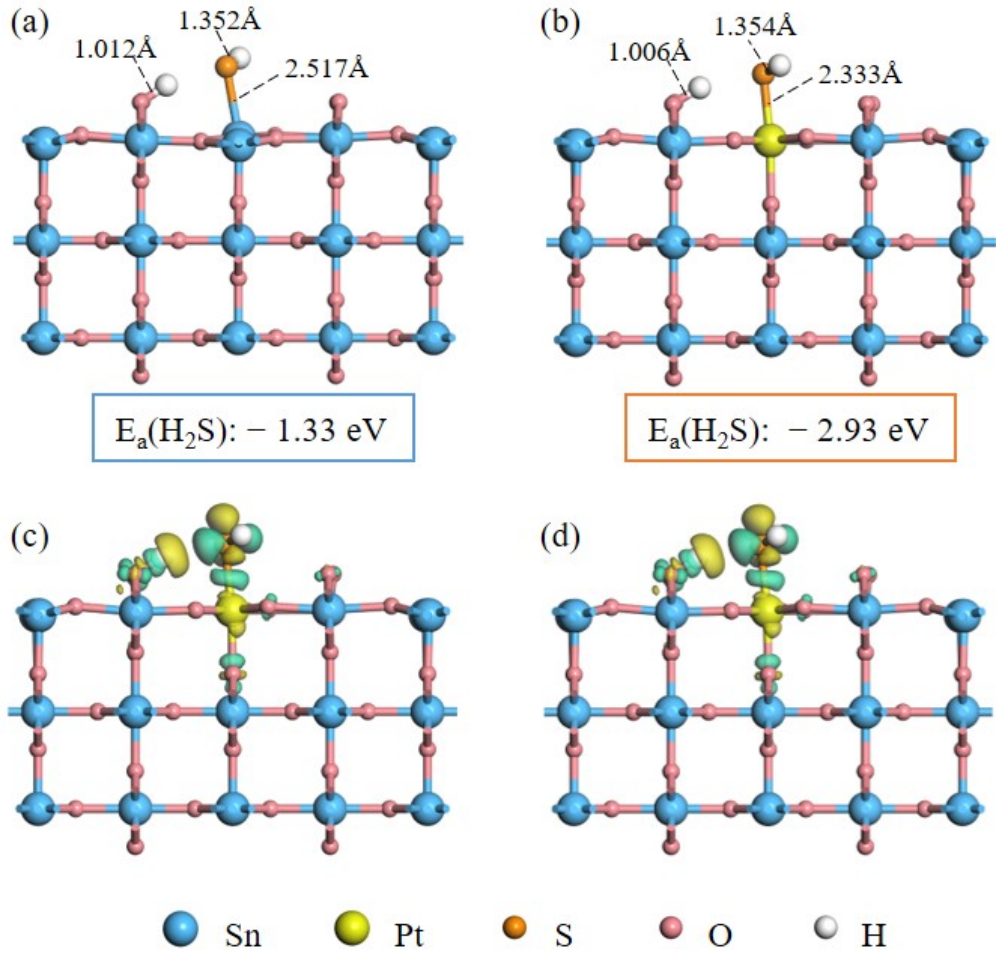



**Figure 7.** The optimized adsorption configurations of $H_2S$ on (**a**) pristine $SnO_2$(110) and (**b**) $Pt_{Sn5c}/SnO_2$(110), the three-dimensional charge-density-difference plot of (**c**) $H_2S$ on $SnO_2$(110), and (**d**) $H_2S$ on $Pt_{Sn5c}/SnO_2$(110).

This stronger local interaction is also reflected in the adsorption energy. The adsorption energy of $H_2S$ on $Pt_{Sn5c}/SnO_2$(110) is −2.93 eV, which is more negative than that on

pristine $SnO_2$(110) (−1.33 eV). This result demonstrates that Pt substitution at the Sn5c site strengthens the interaction between $H_2S$ and the $SnO_2$(110) surface and improves the adsorption capability toward $H_2S$. Together with the shorter Pt–S distance, the adsorption-energy result indicates that the Pt site acts as a more favorable adsorption center for $H_2S$, which can facilitate effective gas capture and subsequent interfacial electronic interaction.

The interfacial charge redistribution induced by $H_2S$ adsorption was visualized by charge density difference analysis (Figure 7c,d). Distinct charge-accumulation and charge-depletion regions are observed around the Sn5c and $Pt_{Sn5c}$ site, the adsorbed S atom, and the Sn–S and Pt–S interaction region after $H_2S$ adsorption. This result reveals substantial interfacial charge redistribution between $H_2S$ and the Sn5c and $Pt_{Sn5c}$ site. The three-dimensional charge-density-difference plot illustrates the spatial reconstruction of the local electron cloud, whereas the two-dimensional sectional map (Figure S6) more clearly shows the charge redistribution between $Pt_{Sn5c}$ and S atoms. Such an interfacial charge-reorganization feature indicates that the Pt–S interaction is accompanied by significant electronic coupling rather than simple physical contact [65,66]. Hirshfeld charge analysis shows that the adsorbed $H_2S$ molecule carries a net positive charge of +0.05e on pristine $SnO_2$(110), indicating an electron transfer of approximately 0.05e from $H_2S$ to the substrate. After Pt modification, the net charge of $H_2S$ increases to +0.11e, suggesting enhanced electron donation from $H_2S$ to the Pt/$SnO_2$ surface. These results indicate that Pt substitution strengthens the interfacial charge transfer and electronic interaction between $H_2S$ and $SnO_2$(110).

Figure 8a compares the total DOS of pristine $SnO_2$(110), $Pt_{Sn5c}/SnO_2$(110), $H_2S$ on $SnO_2$(110), and $H_2S$ on $Pt_{Sn5c}/SnO_2$(110). Compared with pristine $SnO_2$(110), Pt substitution noticeably modifies the electronic-state distribution, particularly in the upper valence region and near the Fermi level, demonstrating that Pt incorporation effectively regulates the local electronic structure of the $SnO_2$(110) surface. After $H_2S$ adsorption, the total DOS of $Pt_{Sn5c}/SnO_2$(110) undergoes further reconstruction, especially through the emergence of new DOS features or distinct peak-shape variations near the Fermi level. In contrast, $H_2S$ adsorption on pristine $SnO_2$(110) produces a relatively weaker DOS perturbation. These results indicate that the Pt-substituted site amplifies the influence of $H_2S$ adsorption on the surface electronic structure and enables more effective modulation of near-Fermi-level states relevant to carrier transport.

The orbital origin of this electronic reconstruction was further examined by analyzing the PDOS of the Pt-d states before and after adsorption, together with the p states of the adsorbed S atom (Figure 8b). On the clean $Pt_{Sn5c}/SnO_2$(110) surface, the Pt-d states are mainly distributed below and around the Fermi level. Upon $H_2S$ adsorption, the Pt-d states are substantially reconstructed and show an overall shift toward higher energies. A new Pt-d-related feature emerges near the Fermi level, while a broad and relatively flat Pt-d distribution appears at approximately −2 eV. Notably, the S-p states of adsorbed $H_2S$ exhibit clear energetic overlap and corresponding spectral features with the adsorbed Pt-d states around −2 eV and near the Fermi level. Since the S-p curve is plotted in a mirrored manner, this correspondence directly indicates pronounced electronic coupling and hybridization between Pt-d and S-p orbitals. Such Pt-d/S-p hybridization is consistent with the charge redistribution observed around the Pt–S interaction region and demonstrates that the Pt-substituted site provides an effective electronic-interaction channel for $H_2S$ adsorption [67,68].

In addition, the adsorption energies of the interfering gases ($NH_3$, $CH_3COCH_3$, CO, $CH_3OH$, HCHO, and $C_2H_5OH$) on $Pt_{Sn5c}/SnO_2$(110) were calculated (Figure S7). $H_2S$ exhibits the most negative adsorption energy (−2.93 eV) among all the tested gases (−1.37 to −2.44 eV), indicating that $H_2S$ is preferentially adsorbed at the Pt sites, which is consistent with the high selectivity of the Pt/$SnO_2$ sensor toward $H_2S$ (Figure 5c).

Taken together, the structural, adsorption-energy, charge, and DOS/PDOS analyses consistently demonstrate that Pt substitution at the Sn5c site enhances the adsorption and electronic response of the $SnO_2$(110) surface toward $H_2S$. The $Pt_{Sn5c}$ site interacts strongly with the S atom of $H_2S$ through interfacial charge transfer and Pt-d/S-p orbital hybridization, which reconstructs the electronic states near the Fermi level. Pt therefore serves not only as a preferential adsorption site for $H_2S$ but also as an electronic coupling center between the gas molecule and the $SnO_2$ substrate [69]. These theoretical results agree with the sensing mechanism discussed above and support the enhanced response and selectivity of the Pt/$SnO_2$ sensor toward $H_2S$ (Figures 4c and 5b,c).

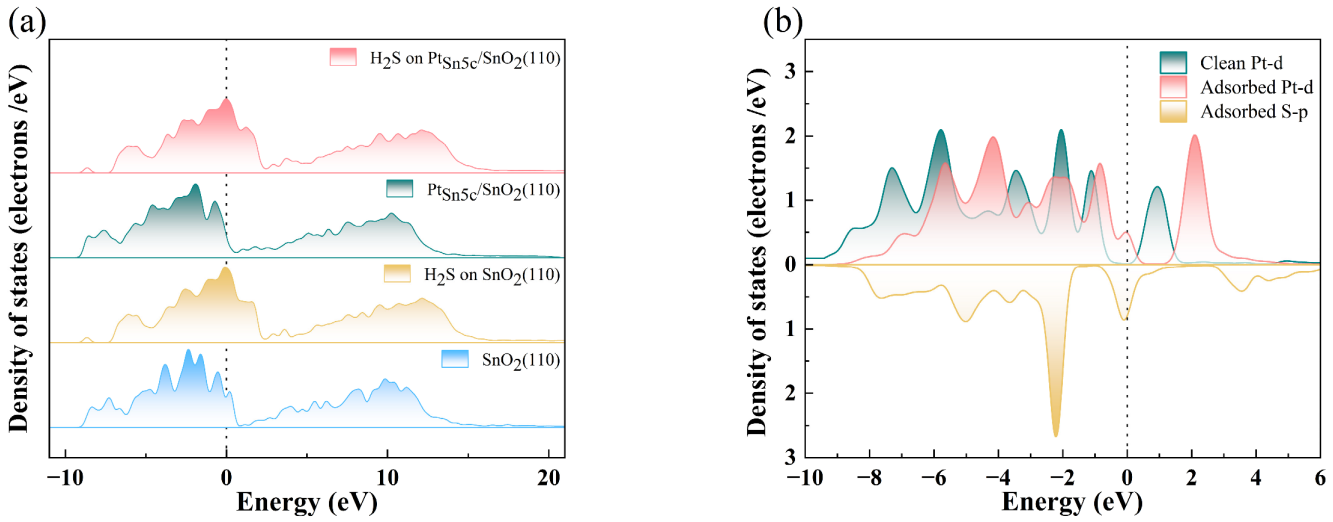



**Figure 8.** (**a**) The total DOS of pristine $SnO_2$(110), $Pt_{Sn5c}$/$SnO_2$(110), $H_2S$ on $SnO_2$(110), and $H_2S$ on $Pt_{Sn5c}$/$SnO_2$(110), (**b**) the PDOS of Pt-d states before and after $H_2S$ adsorption, together with the p states of the adsorbed S atom.

### *3.5. Practical Application*

As illustrated in Figure 9a, the physical appearance of the shrimp deteriorated markedly across four distinct stages: fresh (0–2 h), sub-fresh (4–6 h), spoiled (8–12 h), and severely spoiled (24 h). The initial translucent body and tight shell structure progressively degraded into noticeable tissue softening, head detachment, and distinct melanosis accompanied by intense reddening, which stems from astaxanthin oxidation and enzymatic breakdown [70]. Dynamic headspace testing results presented in Figure 9b demonstrate that the sensor resistance modulation remained negligible during the initial 0–4 h, followed by a discernible response signal at 6 h and a marked increase after 8 h, culminating in a response value of 35.18 at 24 h. This response trend is consistent with the progression of shrimp spoilage, during which microbial and enzymatic processes can generate volatile compounds, including $H_2S$ [7,71]. To provide a reference for interpreting the sensor response, we compared its temporal changes with the pH, color, and sensory indicators measured during the same storage period (Figure 9c). Shrimp pH increased from 6.50 to 8.25, while ΔE and $a^*$ increased from 0.0 to 38.7 and from 1.35 to 20.06, respectively, and the sensory score decreased from 9.8 to 0.5. Notably, the sensor exhibited a discernible response at 6 h and a marked increase after 8 h, coinciding with the deterioration indicated by these independent freshness measures. Thus, rather than relying solely on the expected increase in gas-sensor response during spoilage, the combined results support the potential of the 2 wt% Pt/$SnO_2$ HNTSs sensor for non-destructive shrimp freshness monitoring.

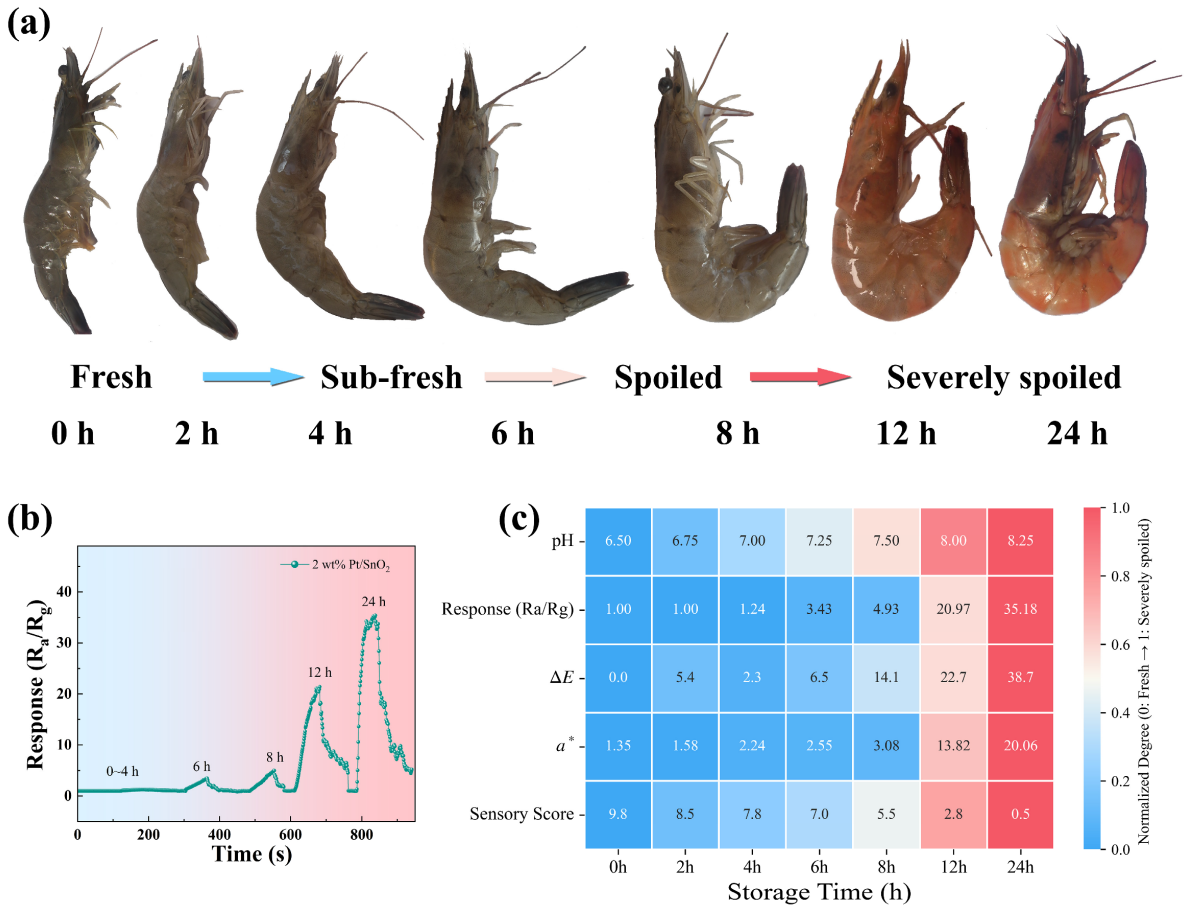



**Figure 9.** Shrimp freshness monitoring with 2 wt% Pt/$SnO_2$ HNTSs sensor at 350 °C. (**a**) Morphological stages of shrimp spoilage. (**b**) Dynamic response curves to headspace gases over time. (**c**) Heatmap of freshness indicators and normalized deterioration levels.

## 4. Conclusions

In summary, Pt-functionalized $SnO_2$ HNTSs were prepared via single-nozzle electrospinning followed by thermal calcination and evaluated for $H_2S$ sensing. Functionalization with Pt significantly improved the $H_2S$ sensing performance compared to pristine $SnO_2$. At an operating temperature of 350 °C, the sensor exhibited a response of 567.1 toward 50 ppm $H_2S$, an 11.9-fold increase relative to pristine $SnO_2$. It also showed an experimental detection limit of 200 ppb, rapid response–recovery kinetics (~1 s and 150 s), good selectivity, and long-term stability. Experimental characterizations and DFT calculations indicated that the enhanced sensing performance is attributable to the accessible gas-diffusion pathways of the hollow nanotubular structure, as well as the Pt-induced promotion of $H_2S$ adsorption and interfacial electronic modulation. During shrimp storage at 30 °C, the sensor response increased alongside changes in pH, color difference, and sensory scores; its marked increase at 6–8 h was consistent with the observed deterioration in freshness indicators. This proof-of-concept test supports the potential of the Pt/$SnO_2$ HNTSs sensor for non-destructive shrimp freshness monitoring, while further validation is needed for practical deployment.

**Supplementary Materials:** The following supporting information can be downloaded at https://www.mdpi.com/article/10.3390/chemosensors14100227/s1, Figure S1: Schematic diagram illustrating the sensor fabrication procedure, structural assembly, and gas-sensing measurement system; Figure S2: TGA curve of as-spun precursor nanofibers; Figure S3: EDS spectrum of 2 wt% Pt/$SnO_2$ HNTSs; Figure S4: Dynamic resistance curve of the 2 wt% Pt/$SnO_2$ HNTSs sensor toward trace-level 200 ppb $H_2S$ at 350 °C; Figure S5: The optimized configurations of (a) pristine $SnO_2$(110) and (b)

$Pt_{Sn5c}/SnO_2(110)$; Figure S6: The two-dimensional sectional map of charge-density-difference plot, (a) $H_2S$ on $SnO_2(110)$, and (b) $H_2S$ on $Pt_{Sn5c}/SnO_2(110)$; Figure S7: The adsorption energies of $H_2S$ and the interfering gases on $Pt_{Sn5c}/SnO_2(110)$; Table S1: Overall atomic percentages and relative species ratios of the samples obtained from XPS spectra.

**Author Contributions:** Conceptualization, Q.F. and H.L.; Methodology, Y.Q., H.L., Q.F. and X.W.; Software and DFT Calculations, H.L. and Y.Q.; Investigation, X.W. and Y.Q.; Data curation, Z.W., Y.D. and B.L.; Writing—original draft preparation, B.L. and X.W.; Writing—review and editing, H.L., X.W., Y.Q., B.L., Z.W., Y.D. and Q.F.; Visualization, Y.Q., X.W. and Y.D.; Supervision, H.L. and Q.F.; Funding acquisition, H.L., Z.W., B.L. and Q.F. All authors have read and agreed to the published version of the manuscript.

**Funding:** This work was financially supported by the Science and Technology R&D Joint Fund of Henan Province, funded by the Henan Science and Technology Department (grant numbers 252103810117, 252103810112, 252103810004, and 20250105).

**Institutional Review Board Statement:** Ethical review and approval were waived for this study due to the use of commercially available food samples purchased from a local market, which did not involve live animals or human participants.

**Informed Consent Statement:** Not applicable.

**Data Availability Statement:** The data supporting the findings of this study are available from the corresponding author upon reasonable request.

**Acknowledgments:** The authors would like to thank the editor and reviewers for their assistance and valuable comments. Generative AI (Gemini and DeepSeek) was used exclusively for language polishing, spelling, and grammar corrections to improve the manuscript's readability. No original content, data, or scientific conclusions were generated by the AI. All suggestions were critically reviewed and approved by the authors, who take full responsibility for the entire content.

**Conflicts of Interest:** The authors declare no conflicts of interest.

## Abbreviations

The following abbreviations are used in this manuscript:

| | |
|---|---|
| DFT | Density functional theory |
| DMF | Dimethylformamide |
| DOS | Density of states |
| $E_{ads}$ | Adsorption energy |
| EDS | Energy Dispersive Spectroscopy |
| HNTSs | Hollow Nanotubular Structures |
| $O_C$ | Chemisorbed oxygen |
| $O_{OH}$ | Surface hydroxyl groups |
| $O_W$ | Adsorbed molecular water |
| PAN | Polyacrylonitrile |
| PDOS | partial density of states |
| PVP | Polyvinylpyrrolidone |
| RH | Relative humidity |
| SAED | Selected area electron diffraction |
| SEM | Scanning electron microscopy |
| SMOs | Semiconductor metal oxides |
| Sn5c | Five-coordinated surface Sn atom |
| TEM | Transmission electron microscopy |
| TGA | Thermogravimetric analysis |
| XPS | X-ray photoelectron spectroscopy |
| XRD | X-ray diffraction |

## References


1. Beauchamp, R.O.; Bus, J.S.; Popp, J.A.; Boreiko, C.J.; Andjelkovich, D.A.; Leber, P. A critical review of the literature on hydrogen sulfide toxicity. *Crit. Rev. Toxicol.* **1984**, *13*, 25–97. [CrossRef]
2. Malone Rubright, S.L.; Pearce, L.L.; Peterson, J. Environmental toxicology of hydrogen sulfide. *Nitric Oxide* **2017**, *71*, 1–13. [CrossRef]
3. Hancock, J.T. Hydrogen sulfide and environmental stresses. *Environ. Exp. Bot.* **2019**, *161*, 50–56. [CrossRef]
4. Zhu, S.; Wu, H.; Zeng, M.; Liu, Z.; Wang, Y. The involvement of bacterial quorum sensing in the spoilage of refrigerated *Litopenaeus vannamei*. *Int. J. Food Microbiol.* **2015**, *192*, 26–33. [CrossRef]
5. Yi, S.; Zhu, J.; Fu, L.; Li, J. Tea polyphenols inhibit Pseudomonas aeruginosa through damage to the cell membrane. *Int. J. Food Microbiol.* **2010**, *144*, 111–117. [CrossRef]
6. Jaffrès, E.; Lalanne, V.; Macé, S.; Cornet, J.; Cardinal, M.; Sérot, T.; Dousset, X.; Joffraud, J.-J. Sensory characteristics of spoilage and volatile compounds associated with bacteria isolated from cooked and peeled tropical shrimps using SPME–GC–MS analysis. *Int. J. Food Microbiol.* **2011**, *147*, 195–202. [CrossRef]
7. Dabadé, D.S.; den Besten, H.M.W.; Azokpota, P.; Nout, M.J.R.; Hounhouigan, D.J.; Zwietering, M.H. Spoilage evaluation, shelf-life prediction, and potential spoilage organisms of tropical brackish water shrimp (*Penaeus notialis*) at different storage temperatures. *Food Microbiol.* **2015**, *48*, 8–16. [CrossRef]
8. Li, Y.; Lei, Y.; Tan, Y.; Zhang, J.; Hong, H.; Luo, Y. Efficacy of freeze-chilled storage combined with tea polyphenol for controlling melanosis, quality deterioration, and spoilage bacterial growth of Pacific white shrimp (*Litopenaeus vannamei*). *Food Chem.* **2022**, *370*, 130924. [CrossRef]
9. Yu, M.; Ding, Y.; Du, Q.; Liao, Y.; Miao, W.; Deng, S.; Cullen, P.J.; Zhou, R. Efficacy of Chitosan Oligosaccharide Combined with Cold Atmospheric Plasma for Controlling Quality Deterioration and Spoilage Bacterial Growth of Chilled Pacific White Shrimp (*Litopenaeus vannamei*). *Foods* **2023**, *12*, 1763. [CrossRef]
10. Liu, H.; Dong, Y.; Zhou, H.; Wu, W.; Fan, Z.; Zhao, C.; Zhu, Y. Rapid Non-Destructive Assessment of Aquatic Products Freshness by Gas Sensor Based on Morphology-Controlled $SnO_2$ Hollow Nanosphere. *Foods* **2026**, *15*, 2123. [CrossRef]
11. Ziani, I.; Bouakline, H.; El Guerraf, A.; El Bachiri, A.; Marie-Laure, F.; Sher, F. Integrating AI and advanced spectroscopic techniques for precision food safety and quality control. *Trends Food Sci. Technol.* **2025**, *156*, 104850. [CrossRef]
12. Heffer, S.; Anastasiadi, M.; Nychas, G.-J.; Mohareb, F. Fusion vs. Isolation: Evaluating the Performance of Multi-Sensor Integration for Meat Spoilage Prediction. *Foods* **2025**, *14*, 1613. [CrossRef]
13. Rianjanu, A.; Rayhan, M.A.A.P.; Aulya, M.; Aflaha, R.; Triyana, K.; Taher, T.; Wasisto, H.S. Early Spoilage Detection of Cultured Pacific White Shrimp Using Quartz Crystal Microbalance Gas Sensors. *ChemistrySelect* **2024**, *9*, e202304694. [CrossRef]
14. Uma, S.; Shobana, M.K. Metal oxide semiconductor gas sensors in clinical diagnosis and environmental monitoring. *Sens. Actuators A Phys.* **2023**, *349*, 114044. [CrossRef]
15. Yamazoe, N. New approaches for improving semiconductor gas sensors. *Sens. Actuators B Chem.* **1991**, *5*, 7–19. [CrossRef]
16. Franco, M.A.; Conti, P.P.; Andre, R.S.; Correa, D.S. A review on chemiresistive ZnO gas sensors. *Sens. Actuators Rep.* **2022**, *4*, 100100. [CrossRef]
17. Kang, X.; Deng, N.; Yan, Z.; Pan, Y.; Sun, W.; Zhang, Y. Resistive-type VOCs and pollution gases sensor based on $SnO_2$: A review. *Mater. Sci. Semicond. Process.* **2021**, *138*, 106246. [CrossRef]
18. Rahman, N.; Yang, J.; Zulfiqar; Sohail, M.; Khan, R.; Iqbal, A.; Maouche, C.; Khan, A.A.; Husain, M.; Khattak, S.A.; et al. Insight into metallic oxide semiconductor ($SnO_2$, ZnO, CuO, α-$Fe_2O_3$, $WO_3$)-carbon nitride (g-$C_3N_4$) heterojunction for gas sensing application. *Sens. Actuators A Phys.* **2021**, *332*, 113128. [CrossRef]
19. Mirzaei, A.; Kim, S.S.; Kim, H.W. Resistance-based $H_2S$ gas sensors using metal oxide nanostructures: A review of recent advances. *J. Hazard. Mater.* **2018**, *357*, 314–331. [CrossRef]
20. Li, B.; Zhou, Q.; Peng, S.; Liao, Y. Recent Advances of $SnO_2$-Based Sensors for Detecting Volatile Organic Compounds. *Front. Chem.* **2020**, *8*, 321. [CrossRef]
21. Katoch, A.; Abideen, Z.U.; Kim, J.-H.; Kim, S.S. Influence of hollowness variation on the gas-sensing properties of ZnO hollow nanofibers. *Sens. Actuators B Chem.* **2016**, *232*, 698–704. [CrossRef]
22. Katoch, A.; Choi, S.-W.; Kim, S.S. Effect of the wall thickness on the gas-sensing properties of ZnO hollow fibers. *Nanotechnology* **2014**, *25*, 455704. [CrossRef]
23. Katoch, A.; Sun, G.-J.; Choi, S.-W.; Byun, J.-H.; Kim, S.S. Competitive influence of grain size and crystallinity on gas sensing performances of ZnO nanofibers. *Sens. Actuators B Chem.* **2013**, *185*, 411–416. [CrossRef]
24. Zhu, L.; Wang, J.; Liu, J.; Wang, L.; Yan, W. Applications of Electrospun One-Dimensional Nanomaterials in Gas Sensors. *Prog. Chem.* **2020**, *32*, 344–360. [CrossRef]
25. Lee, J.-H. Gas sensors using hierarchical and hollow oxide nanostructures: Overview. *Sens. Actuators B Chem.* **2009**, *140*, 319–336. [CrossRef]

26. Gao, D.-H.; Yu, Q.-C.; Kebeded, M.A.; Zhuang, Y.-Y.; Huang, S.; Jiao, M.-Z.; He, X.-J. Advances in modification of metal and noble metal nanomaterials for metal oxide gas sensors: A review. *Rare Met.* **2025**, *44*, 1443–1496. [CrossRef]
27. Kou, R.; He, H.; Lu, Y.; Wang, H.; Xu, J.; Song, Y.-Y.; Gao, Z. Boosting $H_2S$ gas sensing performance of metal oxide semiconductors at room-temperature by the electron-extracting effect of Pt nanocluster. *Chem. Eng. J.* **2023**, *476*, 146546. [CrossRef]
28. Chung, J.H.; Lee, E.; Hwang, J.; Park, J.; Hwang, S.; Youm, D.; Shin, D.; Kwon, K.C.; Yim, S.; Lee, W.; et al. Fast-responding ethanol sensor with extremely low detection limit: Influence of Pt film thickness on gas sensing properties. *Appl. Surf. Sci.* **2025**, *690*, 162618. [CrossRef]
29. Sun, Y.-P.; Zhao, Y.-F.; Sun, H.; Jia, F.-C.; Kumar, P.; Liu, B. Synthesis and room-temperature $H_2S$ sensing of Pt nanoparticle-functionalized $SnO_2$ mesoporous nanoflowers. *J. Alloys Compd.* **2020**, *842*, 155813. [CrossRef]
30. Bulemo, P.M.; Cho, H.-J.; Kim, D.-H.; Kim, I.-D. Facile Synthesis of Pt-Functionalized Meso/Macroporous $SnO_2$ Hollow Spheres through in Situ Templating with $SiO_2$ for $H_2S$ Sensors. *ACS Appl. Mater. Interfaces* **2018**, *10*, 18183–18191. [CrossRef]
31. Dong, K.-Y.; Choi, J.-K.; Hwang, I.-S.; Lee, J.-W.; Kang, B.H.; Ham, D.-J.; Lee, J.-H.; Ju, B.-K. Enhanced $H_2S$ sensing characteristics of Pt doped $SnO_2$ nanofibers sensors with micro heater. *Sens. Actuators B Chem.* **2011**, *157*, 154–161. [CrossRef]
32. Kim, M.-H.; Jang, J.-S.; Koo, W.-T.; Choi, S.-J.; Kim, S.-J.; Kim, D.-H.; Kim, I.-D. Bimodally Porous $WO_3$ Microbelts Functionalized with Pt Catalysts for Selective $H_2S$ Sensors. *ACS Appl. Mater. Interfaces* **2018**, *10*, 20643–20651. [CrossRef]
33. Kundu, S.; Sarkar, M.; Shaji, J.; Ghosh, R. Resistive sensor for tetradecane and $H_2S$ based on $SnO_2$ nanoparticles. *Sens. Actuators A Phys.* **2025**, *391*, 116635. [CrossRef]
34. Zhao, C.; Shen, J.; Xu, S.; Wei, J.; Liu, H.; Xie, S.; Pan, Y.; Zhao, Y.; Zhu, Y. Ultra-efficient trimethylamine gas sensor based on Au nanoparticles sensitized $WO_3$ nanosheets for rapid assessment of seafood freshness. *Food Chem.* **2022**, *392*, 133318. [CrossRef]
35. Zhao, Z.; Wang, B.; Wang, Y.; Li, H.; Yang, Z. Fabrication of 2D/2D $Bi_2MoO_6/Ti_3C_2T_x$ heterostructure for room-temperature and humidity-resistant $NH_3$ gas sensor. *Sens. Actuators B Chem.* **2026**, *459*, 139882. [CrossRef]
36. He, Y.; Sun, B.; Jiang, L.; Li, X.; Ma, Y.; Wang, K.; Han, P.; Jin, S. Effect of Ag doping on $SnO_2$ sensing for detecting $H_2S$: A first-principles study. *Vacuum* **2021**, *194*, 110587. [CrossRef]
37. Raju, P.; Rambeloson, J.; Ioannou, D.E.; Motayed, A.; Li, Q. Noble Metal-Decorated $In_2O_3$ for $NO_2$ Gas Sensor: An Experimental and DFT Study. *Chemosensors* **2025**, *13*, 350. [CrossRef]
38. Ruksana, S.; Rajbhar, M.K.; Das, B.; Sharma, C.S.; Kumar, M. $MoSe_2$-Layered Nanosheet Decorated $SnO_2$ Hollow Nanofiber-Based Highly Sensitive and Selective Room Temperature $H_2S$ Gas Sensor. *ACS Appl. Mater. Interfaces* **2024**, *16*, 64264–64275. [CrossRef]
39. Jiao, L.; Tu, C.; Mao, J.; Benjakul, S.; Zhang, B. Impact of theaflavin soaking pretreatment on oxidative stabilities and physico-chemical properties of semi-dried large yellow croaker (*Pseudosciaena crocea*) fillets during storage. *Food Packag. Shelf Life* **2022**, *32*, 100852. [CrossRef]
40. Zhao, Y.; Lan, W.; Shen, J.; Xu, Z.; Xie, J. Combining ozone and slurry ice treatment to prolong the shelf-life and quality of large yellow croaker (*Pseudosciaena crocea*). *LWT* **2022**, *154*, 112615. [CrossRef]
41. Zhang, Z.; Li, X.; Wang, C.; Wei, L.; Liu, Y.; Shao, C. ZnO Hollow Nanofibers: Fabrication from Facile Single Capillary Electrospinning and Applications in Gas Sensors. *Phys. Chem. C* **2009**, *113*, 19397–19403. [CrossRef]
42. Su, P.; Li, W.; Zhang, J.; Xie, X. Chemiresistive gas sensor based on electrospun hollow $SnO_2$ nanotubes for detecting NO at the ppb level. *Vacuum* **2022**, *199*, 100961. [CrossRef]
43. Idriss, H. On the wrong assignment of the XPS O1s signal at 531–532 eV attributed to oxygen vacancies in photo- and electro-catalysts for water splitting and other materials applications. *Surf. Sci.* **2021**, *712*, 121894. [CrossRef]
44. Frankcombe, T.J.; Liu, Y. Interpretation of Oxygen 1s X-ray Photoelectron Spectroscopy of ZnO. *Chem. Mater.* **2023**, *35*, 5468–5474. [CrossRef]
45. Wang, Z.; Mu, Y.; Ding, H.; Wang, Y.; Zhao, J. MOF-Derived $SnO_2$ Gas Sensor Towards Triethylamine. *Chemosensors* **2026**, *14*, 136. [CrossRef]
46. Yin, X.-T.; Yang, Z.-Y.; Dastan, D.; Liu, Y.; Tan, X.-M.; Gao, X.-C.; Zhou, Y.-W.; Li, J.; Ma, X.-G. Sensitivity and selectivity Pt loaded $SnO_2$–$Co_3O_4$ gas sensor for hydrogen detection. *Ceram. Int.* **2023**, *49*, 38717–38725. [CrossRef]
47. Liu, X.; Zhang, J.; Yang, T.; Guo, X.; Wu, S.; Wang, S. Synthesis of Pt nanoparticles functionalized $WO_3$ nanorods and their gas sensing properties. *Sens. Actuators B Chem.* **2011**, *156*, 918–923. [CrossRef]
48. Phuoc, P.H.; Hung, C.M.; Van Toan, N.; Van Duy, N.; Hoa, N.D.; Van Hieu, N. One-step fabrication of $SnO_2$ porous nanofiber gas sensors for sub-ppm $H_2S$ detection. *Sens. Actuators A Phys.* **2019**, *303*, 111722. [CrossRef]
49. Qi, G.; Lu, X.; Yuan, Z. Improved $H_2S$ gas sensing properties of ZnO nanorods via decoration of nano-porous $SiO_2$ thin layers. *RSC Adv.* **2016**, *6*, 45660–45663. [CrossRef]
50. Yang, T.; Yang, Q.; Xiao, Y.; Sun, P.; Wang, Z.; Gao, Y.; Ma, J.; Sun, Y.; Lu, G. A pulse-driven sensor based on ordered mesoporous $Ag_2O/SnO_2$ with improved $H_2S$-sensing performance. *Sens. Actuators B Chem.* **2016**, *228*, 529–538. [CrossRef]
51. Li, H.; Xu, J.; Zhu, Y.; Chen, X.; Xiang, Q. Enhanced gas sensing by assembling Pd nanoparticles onto the surface of $SnO_2$ nanowires. *Talanta* **2010**, *82*, 458–463. [CrossRef]

52. Shin, J.; Hwang, J.Y.; Kim, C.; Park, J.; Roh, J.W.; Choi, S.-W.; Jin, C.; Choi, M.S. $H_2S$ gas sensing enhancement of Au-decorated $SnO_2$ nanospheres synthesized using hydrothermal and microwave methods. *Sens. Actuators Rep.* **2024**, *8*, 100246. [CrossRef]
53. Akbari-Saatlu, M.; Procek, M.; Mattsson, C.; Thungström, G.; Törndahl, T.; Li, B.; Su, J.; Xiong, W.; Radamson, H.H. Nanometer-Thick ZnO/$SnO_2$ Heterostructures Grown on Alumina for $H_2S$ Sensing. *ACS Appl. Nano Mater.* **2022**, *5*, 6954–6963. [CrossRef]
54. Yang, J.-H.; Yuan, K.-P.; Zhu, L.-Y.; Hang, C.-Z.; Li, X.-X.; Tao, J.-J.; Ma, H.-P.; Jiang, A.-Q.; Lu, H.-L. Facile synthesis of α-$Fe_2O_3$/ZnO core-shell nanowires for enhanced $H_2S$ sensing. *Sens. Actuators B Chem.* **2019**, *307*, 127617. [CrossRef]
55. Park, S.; Park, S.; Jung, J.; Hong, T.; Lee, S.; Kim, H.W.; Lee, C. $H_2S$ gas sensing properties of CuO-functionalized $WO_3$ nanowires. *Ceram. Int.* **2014**, *40*, 11051–11056. [CrossRef]
56. Zhang, Y.; Han, S.; Wang, M.; Liu, S.; Liu, G.; Meng, X.; Xu, Z.; Wang, M.; Qiao, G. Electrospun Cu-doped $In_2O_3$ hollow nanofibers with enhanced $H_2S$ gas sensing performance. *J. Adv. Ceram.* **2022**, *11*, 427–442. [CrossRef]
57. Zheng, L.; Bi, W.; Jin, Z.; Liu, S. Synthesis of hierarchical shell-core $SnO_2$ microspheres and their gas sensing properties. *Chin. Chem. Lett.* **2020**, *31*, 2083–2086. [CrossRef]
58. Ji, H.; Zeng, W.; Li, Y. Gas sensing mechanisms of metal oxide semiconductors: A focus review. *Nanoscale* **2019**, *11*, 22664–22684. [CrossRef]
59. Zhang, B.; Wang, M.; Lu, Q.; Xiao, Y.; Shen, H.; Ni, Y.; Liu, Y.; Song, H. Pt/PtO sensitized $WO_3$ nanowires and their enhanced triethylamine gas sensing. *Microchem. J.* **2026**, *224*, 117720. [CrossRef]
60. Dong, Z.; Hu, Q.; Gao, T.; Wang, J.; Kong, J.; Li, J.; Mao, L.; Wu, C.; Xu, J. Confining isolated Pt atoms into the porous $SnO_2$ for efficient gas sensing. *Ceram. Int.* **2024**, *50*, 22220–22231. [CrossRef]
61. Zhou, Q.; Xu, L.; Umar, A.; Chen, W.; Kumar, R. Pt nanoparticles decorated $SnO_2$ nanoneedles for efficient CO gas sensing applications. *Sens. Actuators B Chem.* **2017**, *256*, 656–664. [CrossRef]
62. Guo, X.; Zhang, J.; Ni, M.; Liu, L.; Lian, H.; Wang, H. Comparison of gas sensing properties based on hollow and porous α-$Fe_2O_3$ nanotubes. *J. Mater. Sci. Mater. Electron.* **2016**, *27*, 11262–11267. [CrossRef]
63. Sharma, N.; Choudhury, S.P. First-principles study of metal oxide semiconductors for gas sensing applications: A brief review. *Mod. Phys. Lett. B* **2023**, *38*, 2342012. [CrossRef]
64. Liu, Y.; Xu, C.; Gu, F.L. Unraveling the enhancement mechanisms of $H_2S$ sensing on a $SnO_2$ surface: An ab initio perspective. *Phys. Chem. Chem. Phys.* **2020**, *22*, 15006–15012. [CrossRef]
65. Xu, K.; Liao, N.; Zheng, B.; Zhou, H. Adsorption and diffusion behaviors of $H_2$, $H_2S$, $NH_3$, CO and $H_2O$ gases molecules on $MoO_3$ monolayer: A DFT study. *Phys. Lett. A* **2020**, *384*, 126533. [CrossRef]
66. Keshtkar, S.; Rashidi, A.; Kooti, M.; Askarieh, M.; Pourhashem, S.; Ghasemy, E.; Izadi, N. A novel highly sensitive and selective $H_2S$ gas sensor at low temperatures based on $SnO_2$ quantum dots-$C_{60}$ nanohybrid: Experimental and theory study. *Talanta* **2018**, *188*, 531–539. [CrossRef]
67. Zhou, L.; Yu, S.; Yang, Y.; Li, Q.; Li, T.; Zhang, D. Adsorption of gas molecules ($NH_3$, $C_2H_6O$, $C_3H_6O$, CO, $H_2S$) on a noble metal (Ag, Au, Pt, Pd, Ru)-doped $MoSe_2$ monolayer: A first-principles study. *New J. Chem.* **2021**, *45*, 12367–12376. [CrossRef]
68. Wanbayor, R.; Ruangpornvisuti, V. A periodic DFT study on binding of Pd, Pt and Au on the anatase $TiO_2$ (001) surface and adsorption of CO on the $TiO_2$ surface-supported Pd, Pt and Au. *Appl. Surf. Sci.* **2012**, *258*, 3298–3301. [CrossRef]
69. Jung, G.; Ju, S.; Choi, K.; Kim, J.; Hong, S.; Park, J.; Shin, W.; Jeong, Y.; Han, S.; Choi, W.Y.; et al. Reconfigurable Manipulation of Oxygen Content on Metal Oxide Surfaces and Applications to Gas Sensing. *ACS Nano* **2023**, *17*, 17790–17798. [CrossRef]
70. Bougatef, A. Trypsins from fish processing waste: Characteristics and biotechnological applications—Comprehensive review. *J. Clean. Prod.* **2013**, *57*, 257–265. [CrossRef]
71. Shaalan, N.M.; Ahmed, F.; Saber, O.; Kumar, S. Gases in Food Production and Monitoring: Recent Advances in Target Chemiresistive Gas Sensors. *Chemosensors* **2022**, *10*, 338. [CrossRef]


**Disclaimer/Publisher's Note:** The statements, opinions and data contained in all publications are solely those of the individual author(s) and contributor(s) and not of MDPI and/or the editor(s). MDPI and/or the editor(s) disclaim responsibility for any injury to people or property resulting from any ideas, methods, instructions or products referred to in the content.